



**HAL**  
open science

## Magnetic excitations beyond the single- and double-magnons

Hebatalla Elnaggar, Abhishek Nag, Maurits Haverkort, Mirian Garcia-Fernandez, Andrew Walters, Ru-Pan Wang, Ke-Jin Zhou, Frank de Groot

► **To cite this version:**

Hebatalla Elnaggar, Abhishek Nag, Maurits Haverkort, Mirian Garcia-Fernandez, Andrew Walters, et al.. Magnetic excitations beyond the single- and double-magnons. *Nature Communications*, 2023, 14 (1), pp.2749. 10.1038/s41467-023-38341-8 . hal-04097591

**HAL Id: hal-04097591**

**<https://hal.sorbonne-universite.fr/hal-04097591>**

Submitted on 15 May 2023

**HAL** is a multi-disciplinary open access archive for the deposit and dissemination of scientific research documents, whether they are published or not. The documents may come from teaching and research institutions in France or abroad, or from public or private research centers.

L'archive ouverte pluridisciplinaire **HAL**, est destinée au dépôt et à la diffusion de documents scientifiques de niveau recherche, publiés ou non, émanant des établissements d'enseignement et de recherche français ou étrangers, des laboratoires publics ou privés.

## 1 Title

2 Magnetic excitations beyond the single- and double-magnons

## 4 Author list

5 Hebatalla Elnaggar,<sup>1,2\*</sup> Abhishek Nag,<sup>3</sup> Maurits W. Haverkort,<sup>4</sup> Mirian Garcia-Fernandez,<sup>3</sup>  
6 Andrew Walters,<sup>3</sup> Ru-Pan Wang,<sup>1,5</sup> Ke-Jin Zhou,<sup>3\*</sup> Frank de Groot<sup>1\*</sup>

## 7 Affiliations

8 <sup>1</sup>Debye Institute for Nanomaterials Science, Utrecht University, 3584 CA Utrecht, The  
9 Netherlands.

10 <sup>2</sup>Institute of Mineralogy, Physics of Materials and Cosmochemistry, CNRS, Sorbonne University,  
11 4 Place Jussieu, 75005 Paris, France.

12 <sup>3</sup>Diamond Light Source, Harwell Campus, Didcot OX11 0DE, United Kingdom.

13 <sup>4</sup>Heidelberg University, Philosophenweg 19, 69120 Heidelberg, Germany.

14 <sup>5</sup>Department of Physics, University of Hamburg, Luruper Chaussee 149, G610, 22761 Hamburg,  
15 Germany.

## 17 Abstract

18 A photon carrying one unit of angular momentum can change the spin angular momentum of a  
19 magnetic system with one unit ( $\Delta M_s = \pm 1$ ) at most. This implies that a two-photon scattering process  
20 can manipulate the spin angular momentum of the magnetic system with a maximum of two units.  
21 Herein we describe a triple magnon excitation in  $\alpha$ -Fe<sub>2</sub>O<sub>3</sub>, which contradicts this conventional  
22 wisdom that only 1- and 2-magnon excitations are possible in a resonant inelastic x-ray scattering  
23 experiment. We observe an excitation at exactly three times the magnon energy, along with  
24 additional excitations at four and five times the magnon energy, suggesting quadruple and quintuple  
25 magnons as well. Guided by theoretical calculations, we reveal how a two-photons scattering  
26 process can create exotic higher-rank magnons and the relevance of these quasiparticles for  
27 magnon-based applications.

## 28 Introduction

29 Understanding how to control the spin degree of freedom is a cornerstone for several hot topics of  
30 contemporary magnetism research, including ultrafast magnetism and magnonics. The main idea  
31 behind magnonics is to use the elementary magnetic excitations (magnons) for information transfer  
32 and processing. Magnons are bosonic quasiparticles and are the quanta of magnetic oscillations of  
33 systems with periodically ordered magnetic moments (1). A magnon is classically depicted as a  
34 phase-coherent precession of microscopic vectors of magnetization in a magnetic medium. When  
35 a magnon propagates through a magnetic medium, no electrical charge transport is involved and  
36 hence no electrical losses take place. This is the key advantage of using magnons as information  
37 carriers. The energy of magnons range typically in the terahertz range (in the order of 1 to 25 THz,  
38 i.e., 5 to 100 meV). The magnon frequency has an important impact on the performance of magnon-  
39 based devices because the larger the excitation frequency, the faster are the magnons, at least for a  
40 fraction of the magnon band. This means that the use of high-frequency (terahertz) magnons could  
41 provide a great opportunity for the design of ultrafast devices (2). Antiferromagnets represent an  
42 appealing playground for the search for new channels of high frequency, long-lived magnons  
43 paving the way towards ultrafast magnon-based devices (3,4).

44 Collective excitations such as magnons can be effectively measured using  $2p3d$  resonant inelastic  
45 x-ray scattering (RIXS) (5). Here a  $2p$  core electron is resonantly excited from its initial state to the  
46 empty  $3d$  orbitals through an electrical dipole transition. This excited state contains a localized  
47 core-hole that has a life time of  $\sim 100$  fs determined by Auger decay. The radiative decay of a  $2p$

48 core hole brings the system back to the ground state, as well as final states including low-energy  
49 excitations. In 1998, it was proposed that  $2p3d$  RIXS can be used to measure magnetic excitations,  
50 referred to as spin-flip by de Groot and coworkers (5). Consider a magnetic  $3d^9$  system where the  
51 hole resides in the  $dz^2$  orbital and is spin-up. An incoming photon with the correct energy and  
52 polarization can excite a  $2p$  core-electron into the empty  $dz^2$  spin-up hole leading to a  $2p^53d^{10}$   
53 intermediate state. While the spin-orbit interaction at the  $3d$  shell is in the order of 100 meV, it is  $\sim$   
54 12 eV for the  $2p$  shell: This implies that spin and orbital momenta are mixed in the intermediate  
55 state, so neither is a good quantum number and only the total angular momentum is defined.  
56 Therefore, the intermediate state can decay to a  $3d^9$  with a  $dz^2$  spin-down hole final state. This  
57 excitation is referred to as a spin-flip excitation because when one compares the initial state with  
58 the final state, one finds that the only change between both is the spin projection from up to down  
59 and a corresponding counter change in the photon angular momentum. In a magnetic material such  
60 as  $\alpha$ -Fe<sub>2</sub>O<sub>3</sub>, the magnetic excitations are nonlocal collective excitations in the form of magnons. A  
61 magnon excitation is commonly interpreted to originate from a local single-site spin-flip RIXS  
62 process. This description is widely used because the intermediate state in a  $2p3d$  RIXS experiment  
63 is strongly localized due to the  $2p$  core-hole and hence such a local picture is very useful to describe  
64 many aspects of the RIXS process. However, the final state excited by RIXS is not necessarily  
65 localized and can be a collective excitation such as magnons in a magnetic material. The way to  
66 reconcile both the local single-site and collective aspects of RIXS is to realize that the incident  
67 photon can be scattered at any equivalent site, leading to a final state that is a superposition of spin-  
68 flips at equivalent sites. Such a final state carries a nonlocal magnetic excitation and represents the  
69 magnon density of states as also confirmed by detailed comparison to inelastic neutron scattering  
70 (INS) data (6). As a photon in the x-ray regime has a non-negligible linear momentum, one can also  
71 measure the dispersion of magnons when spin-flip scattering is allowed in RIXS. This realization  
72 has been the main motivation behind the development of high resolution resonant inelastic x-ray  
73 scattering (RIXS) beamlines, with the goal to study the spin dynamics of (pseudo)spin  $S = 1/2$   
74 materials such as cuprates and iridates (7-10).

75 Spin-half systems represent a special case as only transitions from  $M_s = -1/2$  to  $M_s = 1/2$  are allowed  
76 on a single atomic site. These magnons propagate a change of one unit of angular momentum and  
77 are similar to the magnons observed by other techniques such as INS and Raman scattering (11).  
78 We will refer to these magnons as conventional single-magnons. Whereas it is only possible to flip  
79 a single spin at a local single magnetic site for cuprates and iridates resulting in a collective single-  
80 magnon excitation in the material, the nickelates can theoretically present single and double spin-  
81 flip excitations. This is because the Ni<sup>2+</sup> is  $3d^8$  with  $S = 1$  and hence excitations between  $M_s = 1, 0,$   
82  $-1$  are possible on a single site leading to single- and double-magnons in the extended system. RIXS  
83 measurements on NiO has confirmed the presence of single ( $\Delta M_s = 1$ ) and double-magnons ( $\Delta M_s$   
84  $= 2$ ) in the system (12,13). We point out that double-magnons are different from bimagnons  
85 observed in cuprates. A double-magnon is a  $\Delta M_s = 2$  transition, while a bimagnon is composed of  
86 two single-magnons, one changing the spin projection with  $+1$  (i.e.,  $\Delta M_s = 1$ ) and the other with  $-1$   
87 (i.e.,  $\Delta M_s = -1$ ) giving rise to a combined  $\Delta M_s = 0$  transition (14).

88 While it is clear that for high spin Ni<sup>2+</sup> ions in NiO possessing two unpaired  $3d$  electrons that only  
89 two spins can change their angular momenta (i.e., excitations between  $M_s = 1, 0, -1$ ), the situation  
90 is more complicated for a high spin  $3d^5$  ion in a magnetic system. In this case, there are conceptually  
91 five spins that could be locally reversed resulting in magnons carrying a change of angular  
92 momentum of up to 5 units in the extended system (i.e., local spin-flip excitations between  $M_s =$   
93  $5/2, 3/2, 1/2, -1/2, -3/2, 5/2$  leading to a higher-rank magnon final state that is a superposition of  
94 higher-rank spin-flips at equivalent sites). This raises the fundamental question: Is it possible to  
95 change the spin angular momentum of a system with an amount greater than the change in the x-  
96 ray photon angular momentum of the RIXS experiment?

97 Here we provide experimental data capable of answering this question by measuring the low-energy  
98 magnon spectrum of an  $\alpha$ -Fe<sub>2</sub>O<sub>3</sub> single crystal at the ultra-high resolution I21 RIXS setup ( $\Delta E = 32$   
99 meV) at Diamond Light Source (15). Guided by theory, we show that the crystal lattice acts as a  
100 reservoir of angular momentum which provides the extra angular momentum required to excite the  
101 higher-rank magnons (i.e., beyond single- and double-magnons). We developed a low-energy  
102 effective operator that describes the higher-rank magnons and derived simple selection rules that  
103 can be used to predict the best experimental settings for exciting the higher-rank magnons.

## 104 Results

105 The antiferromagnet  $\alpha$ -Fe<sub>2</sub>O<sub>3</sub> is an ideal material to initiate this kind of study because the ground  
106 state of Fe<sup>3+</sup> has the maximum number of unpaired electrons for the *d* orbitals providing a platform  
107 to test the maximum number of possible single-site spin-flip excitations. Furthermore, the <sup>6</sup>A<sub>1</sub>  
108 orbital singlet ground state makes a clean case to study solely spin excitations without any orbital  
109 contribution.

110 Figure 1(a) shows the Fe ions in the unit cell of  $\alpha$ -Fe<sub>2</sub>O<sub>3</sub>. The exchange coupling is dominantly  
111 antiferromagnetic with the Néel temperature  $T_N$  of  $\sim 950$  K. In addition to the Néel transition,  $\alpha$ -  
112 Fe<sub>2</sub>O<sub>3</sub> exhibits another magnetic transition, referred to as the Morin transition ( $T_M$  of  $\sim 250$  K)  
113 where below  $T_M$  it is purely antiferromagnetic. We performed our measurements at 13 K ( $T < T_M$ )  
114 in the collinear antiferromagnetic phase. An exemplary L<sub>3</sub> x-ray absorption spectrum (XAS) is  
115 shown in Figure 1(b) where we find two main peaks (labelled E<sub>1</sub> and E<sub>2</sub> where this splitting is due  
116 to the crystal field) exhibiting the expected x-ray magnetic linear dichroism signal in line with  
117 previous literature (16-18).

118 The RIXS spectrum measured at E<sub>1</sub> is shown in Figure 1(c). The elastic line is observed at zero  
119 energy transfer where the final state preserves the initial state spin orientation. A cascade of energy  
120 transfer peaks can be seen at 100, 200, 300, 400 and 500 meV. The first energy transfer peak can  
121 be assigned to a single-magnon excitation. This agrees well with the observation from INS  
122 experiments, where an optical nearly non-dispersing mode is observed at  $\sim 100$  meV (19). The  
123 single-magnon excitation propagates a change of angular momentum of  $\Delta M_s = 1$ . The second  
124 energy transfer peak appears at double the energy of the single-magnon and can be assigned to a  
125 double-magnon excitation ( $\Delta M_s = 2$ ) similar to the double-magnon excitation observed in NiO  
126 (12,13). The most remarkable feature in our results is the ability of the two-photon RIXS process  
127 to excite higher-rank magnons at 3 times, 4 times and potentially at 5 times the energy of a single-  
128 magnon (zoom in Figure 1(d) and its first derivative in (e)). These higher-rank magnons propagate  
129 these multiples of angular momentum. We provide the details of the fitting and the full energy loss  
130 spectra at two incident energies in the materials and methods in Figures S1, S2 and S3.

131 We measured the angular dependence of the single-, double- and triple-magnons by rotating the  
132 sample in the azimuthal ( $\alpha$ ) direction to decipher the nature of the transitions involved (see Figure  
133 2). Conceptually, one expects that the angular behavior of the higher-order magnons differs from  
134 the single-magnon as the angular momentum selection rules are different ( $\Delta M_s = 1, 2, 3$  involves  
135 a dipolar, quadrupolar and hexapolar spin-flip process respectively). This is confirmed by  
136 comparing the angular behavior in panels (a), (b) and (c) of Figure 2 where the magnitudes of the  
137 transitions are reduced approximately with an order of magnitude as we move from single- to  
138 double- to triple-magnons, in addition to the change of the angular profile. The angular dependent  
139 RIXS of these excitations however, did not show any noticeable dispersion (see Figure S4). The  
140 parent single-magnon is an optical mode that shows negligible dispersion according to INS  
141 measurements which agrees with our measurement (19).

142 **Discussion**

143 The implication of our experimental observation is that the two-photon RIXS process can exchange  
 144 five units of angular momenta with a single magnetic-site. This is an unexpected result because the  
 145 selection rule for a dipole transition in presence of strong spin-orbital coupling is that the change  
 146 of the total angular momentum ( $\Delta M_j$ ) is equal to 0 or  $\pm 1$ . This means that for a dipole-in ( $2p \rightarrow 3d$   
 147 transition), dipole-out ( $3d \rightarrow 2p$  transition)  $2p3d$  RIXS process, possible transition should involve  
 148  $\Delta M_j = 0, \pm 1, \pm 2$  giving rise to only single- and double-magnons. We performed multiplet ligand  
 149 field theory calculations for  $\text{Fe}^{3+}$   $L_3$ -edge RIXS (see Figure 3(a)) which confirms that only single-  
 150 and double- magnons are expected to be observed and is in line with previous work on NiO (12,13).  
 151 It is essential to examine the interaction terms of the model Hamiltonian responsible for the single-  
 152 and double-magnons to find the origin behind the higher-rank magnons in  $\alpha\text{-Fe}_2\text{O}_3$ .

$$H = \sum_k f_k F^k + \sum_k g_k G^k + \sum_i l_i \cdot s_i + J_{exch}(n, S) \quad (1)$$

153 The model Hamiltonian used for the calculation is given by equation (1). The  $J_{exch}(n, S)$  term is  
 154 the mean-field super exchange interaction term that determines the energy of the single-magnon.  
 155 The spin orbit coupling is given by the  $\sum_i l_i \cdot s_i$  term and is responsible for the spin-flip process by  
 156 mixing the orbital and spin degrees of freedom and enables the observation of single-magnons as  
 157 detailed in the work of de Groot *et. al.* (5). The double-magnon is enabled through the intra-atomic  
 158 Coulomb exchange given by  $\sum_k f_k F^k + \sum_k g_k G^k$ .  $F_k(f_k)$  and  $G_k(g_k)$  are the Slater–Condon  
 159 parameters for the radial (angular operators) part of the direct and exchange Coulomb interactions,  
 160 respectively. The intra-atomic Coulomb exchange interaction strongly couples the valence and core  
 161 electrons implying that the spin angular momentum of both the core and valence orbitals are no  
 162 longer a good quantum number, effectively leading to  $\Delta M_s = 0, 1, \text{ and } 2$  excitations.

163 It is inevitable to conclude that the higher-rank magnons have a different origin compared to the  
 164 single- and double-magnons reported in previous work (12, 13, 20) and a mechanism that allows  
 165 the exchange of higher angular momenta is needed. This apparent contradiction can be reconciled  
 166 by realizing that the angular momenta of electrons only is not a conserved quantum number in real  
 167 crystals (21). The crystal lattice can exchange angular momentum with the electrons providing the  
 168 extra angular momentum required for higher-rank magnons involving  $\Delta M_s > 2$ . We performed a  
 169 full-multiplet ligand field theory calculation for  $\text{Fe}^{3+}$   $L_3$ -edge RIXS including the effect of the  
 170 crystal lattice using an effective octahedral crystal field potential (see Figure 3(b)). In addition to  
 171 the single- and double-magnons, triple-, quadruple- and quintuple-magnons are now visible  
 172 confirming that the crystal field potential is the key factor behind the higher-rank excitations as can  
 173 be seen in details in the linear cuts of the RIXS map in Figure 3(c). Here we stress that the higher-  
 174 rank magnons are generated from a single magnetic-site and the role of the crystal lattice can be  
 175 considered as a reservoir of angular momentum supplying the extra angular momentum required.

176 To visualise the role of the crystal lattice, we follow in Figure 4 the fate of an excitation created by  
 177 the absorption, for example, of a circular right polarized photon. We define the polarization of light  
 178 as:  $|R\rangle = \frac{1}{\sqrt{2}}[1, -i, 0]$ ,  $|L\rangle = \frac{1}{\sqrt{2}}[1, i, 0]$  and  $|Z\rangle = [0, 0, 1]$ . The initial state can be represented by the vector  
 179 shown in Figure 4(a) which includes the  $2p$  and  $3d$  orbitals participating in the RIXS process. The  
 180 first two numbers shaded in gray represent the occupation of the  $2p$  spin down (red arrow) and  $2p$   
 181 spin up orbitals (blue arrow) where we take the spin quantization axis to be the  $C_4$  axis of the  
 182 octahedron. The second two numbers shaded in yellow are the  $3d$  spin down (red arrow) and  $3d$   
 183 spin up orbitals (blue arrow) occupation numbers. The projection of the total orbital angular

184 momentum,  $L_z$ , is specified in the subscript of the vector to keep track of the orbital angular  
 185 momentum of the states. This means that the initial state is given by  $(3,3,5,0)_0$ .

186 Upon the absorption of the polarized photon, a spin-up electron can be excited from the  $2p_{-1}$  to the  
 187  $3d_{-2}$  orbital resulting in an intermediate state given by  $(3,2,5,1)_{-1}$  (Figure 4(a)). This intermediate  
 188 state can decay back elastically by emitting a right polarized photon contributing to the elastic RIXS  
 189 peak (Figure 4(b1)). Another possible path is shown in Figure 4(b2) where a  $3d_{-2}^{\uparrow}$  electron scatters  
 190 off the crystal field potential to a  $3d_{-2}^{\uparrow}$  orbital and thereby changes its angular momentum by four  
 191 units. This extra angular momentum provided by the lattice is the key aspect that makes it possible  
 192 to excite higher-rank magnons. A cascade of  $2p$  spin-orbit coupling and  $2p$ - $3d$  exchange interaction  
 193 are required to transfer this orbital angular momentum to spin angular momentum as illustrated in  
 194 panels (c) to (i) of Figure 4. The first pair of  $2p$  spin-orbit coupling and  $2p$ - $3d$  exchange interaction  
 195 changes the intermediate state to  $(3,2,4,2)_2$ . We note that this intermediate state cannot decay to a  
 196 single-magnon excitation as it cannot reach a  $L_z = 0$  final state through a dipole emission. The  
 197 second pair of  $2p$  spin-orbit coupling and  $2p$ - $3d$  exchange interaction changes the intermediate state  
 198 to  $(3,2,3,3)_1$ . Now this intermediate state can decay to a double-magnon excitation either after the  
 199  $2p$  spin-orbit coupling step ( $2p_{-1}^{\downarrow} \rightarrow 3d_{-2}^{\downarrow}$  emitting a left polarized photon - not shown in Figure 4  
 200 for visual clarity) or after the exchange interaction step emitting a left polarized photon (Figure  
 201 4(g1)). A final  $2p$  spin-orbit coupling step is required to changes the intermediate state to  $(2,3,3,3)_0$   
 202 which can finally decay to a triple-magnon by emitting a Z polarized photon (Figure 4(h)).

203 Quadruple and quintuple magnons can be reached by further exchange of angular momentum with  
 204 the lattice followed by cascades of  $2p$  spin-orbit coupling and  $2p$ - $3d$  exchange interaction. In  
 205 contrast, when the crystal-field is not considered, only single- and double-magnons can be excited  
 206 (see the Feynman-diagrams in Figure S5). The transparent Feynman-diagram representation allows  
 207 us to derive simple selection rules for this example: (i) it is not possible to excite single-magnons  
 208 using circular right polarized incoming x-rays, (ii) double-magnons can be selectively observed by  
 209 detecting the left polarized outgoing light. (iii) triple-magnons can be selectively observed by  
 210 detecting the Z polarized outgoing light. The Z polarized light can be experimentally detected by  
 211 placing an extra detector in the vertical plane for example. A full RIXS calculation is shown in  
 212 Figure S6 and confirms the selection rules derived from Figure 4.

213  
 214 We developed a low-energy effective RIXS operator that describes low-energy magnetic  
 215 excitations such as magnons in terms of spin operators based on the work of Haverkort (22). The  
 216 full RIXS cross-section is given by equation (2) where the ground state  $|i\rangle$  is excited by a photon  
 217 described by a dipole transition operator  $T_{\epsilon_i}$  to an intermediate state described by the Hamiltonian  
 218 (H) and decays to all possible final states  $|f\rangle$  emitting a photon described by a dipole transition  
 219 operator  $T_{\epsilon_o}$ .

$$220 \quad RIXS(\omega) \propto \sum_f |\langle f | T_{\epsilon_o}^{\dagger} \frac{1}{\omega_i - H + i\Gamma/2} T_{\epsilon_i} | i \rangle|^2 = \sum_f |\langle f | R_{eff} | i \rangle|^2 \quad (2)$$

221  
 222 The effective operator ( $R_{eff}$ ) removes the intermediate state from the equation by expanding the  
 223 intermediate state Hamiltonian in terms of polynomials of spin operators multiplied by x-ray  
 224 absorption fundamental spectra. The expression of the expansion to the third order is presented in  
 225 the materials and methods and is summarized in Figure 5(a). The spin flip processes resulting in  
 226 magnons can be grouped in order of the spin operator rank: linear (shaded in blue), quadratic  
 227 (shaded in purple) and cubic (shaded in red) operators. The linear spin operators can generate  
 228 single-magnons while the quadratic spin operators generate single- and double-magnons and

229 produce the majority of the RIXS intensity (see Figure 5(b)). Finally, the cubic spin operators can  
230 generate single-, double- and triple-magnons. The main advantage of this expansion is its simple  
231 form that allows one to determine general selection rules depending on the polarization of the  
232 incoming and outgoing light.

233 We computed the angular dependence of the single-, double- and triple-magnons based on this  
234 expansion in Figure 6. Our calculations capture the essential aspects of the experimental angular  
235 dependence where we obtain the correct order of magnitude for the magnons and reproduce the  
236 general angular dependence confirming the nature of the higher-rank magnons (compare Figure 2  
237 to Figure 6). Some deviations of the calculated angular dependence from the experiment could be  
238 to several factors. On the experimental side, our measurements were performed on a bulk single  
239 crystal which is prone to self-absorption and saturation effects. As the RIXS cross-section is a  
240 combination of an absorption (photon-in) process and an emission (photon- out) process, two  
241 geometrical effects have to be taken into account here: the probing depth is dependent on the x-ray  
242 absorption spectroscopy (XAS) cross-section (saturation) and the emitted photons can be re-  
243 absorbed (self-absorption). Consequently, the RIXS intensity is distorted in a bulk crystal according  
244 to the photon energy and the experimental geometry (23). When the sample is rotated, the probing  
245 depth is changed, and the photons emitted at different energies have different escape lengths, hence  
246 distorting the angular dependence. It is difficult to correct for these geometrical energy-dependent  
247 effects because it is affected by the background absorption (which is the off-resonant contribution  
248 from other elements in the sample and in the path of the beam). On the theoretical side, one likely  
249 reason for the deviation could be the fact that the Fe sites in hematite have a small trigonal  
250 distortion. As a first approximation, the trigonal distortion would not change the ground state of  
251  $\text{Fe}^{3+}$  because the singlet  ${}^6\text{A}_1$  ground state does not split. However, the trigonal distortion would  
252 influence the intermediate states, and hence could modify the intensity and consequently the angular  
253 dependence (24). Finally, we point out that ligand field-multiplet theory reduces a full solid to a  
254 local cluster. This means that any Fe-Fe interactions or intercluster hopping are not considered. We  
255 expect that the above approximations can affect the angular dependence (25).

256 The comparison between theory and experiment on  $\alpha\text{-Fe}_2\text{O}_3$  confirms that the cascade of excitations  
257 we observed at triple, quadruple, and quintuple the energy of a single-magnon are higher rank-  
258 magnons that propagate these higher multiples of spin angular momentum. From a fundamental  
259 point of view, the higher-rank magnons can couple differently with the various degrees of freedom  
260 of the system providing a unique platform to investigate magnon interactions. From a technological  
261 point of view, these excitations have higher energies than that of single-magnons and hence are  
262 potentially more thermally robust. We predict that these higher-rank magnons can also be excited  
263 using THz-pulses and can be enhanced using magnonic crystals paving the way towards future  
264 magnonic devices.

## 265 **Methods**

### 266 ***Resonant inelastic x-ray scattering measurements***

267 High-resolution ( $\Delta E = 32$  meV), Fe  $L_3$ -edge resonant inelastic x-ray scattering measurements were  
268 done at the I21 beamline of the Diamond Light Source, United Kingdom. Linear horizontally ( $\pi$ )  
269 or vertically polarized ( $\sigma$ ) x-ray beam was used. The angular dependence was measured by rotating  
270 the sample about the b-axis (referred to as  $\alpha$  rotation) of a polished  $\alpha\text{-Fe}_2\text{O}_3$  single crystal cooled  
271 down to 13 K. The Morin temperature of  $\text{Fe}_2\text{O}_3$  is 220 K. The scattering angle was kept fixed at  
272  $150^\circ$ . The x-ray absorption spectrum (XAS) shown in Figure 1(b) was measured using total electron  
273 yield in the same geometry. The pressure in the experimental chamber was maintained below  $5 \times 10^{-10}$   
274 mbar. The zero-energy transfer position and resolution of the RIXS spectra were determined from  
275 subsequent measurements of elastic peaks from an adjacent carbon tape.

### 276 **Resonant inelastic x-ray scattering data fitting**

277 RIXS data were corrected for self-absorption prior to fitting. The elastic line was fitted with an  
278 energy resolution limited Gaussian lineshape (orange shade, Figure 1(c) and SI Figure 1(a)). The  
279 phonon peaks close to 43 meV and 150 meV were fitted with asymmetric Lorentzian functions  
280 (shown by gray dashed lines) convoluted with the energy resolution. These peaks are clearly visible  
281 in RIXS spectra at E<sub>2</sub> peak of XAS (see inset of SI Figure 1(b)). The five shaded antisymmetric  
282 Lorentzian peaks convoluted with the energy resolution represent the single- (blue), double-  
283 (purple), triple- (red), quadruple- (green) and quintuple- (black) magnon excitations (Figure 1c and  
284 SI Figure 1(a)). While the energy positions up to the quadruple magnon excitation were kept as a  
285 free parameter for fitting, the energy position of the quintuple magnon was fixed to (fitted energy  
286 position of the triple magnon)\*(5/3). See also SI Figure 2 and SI Figure 3 for the low energy fits to  
287 the RIXS data for different  $\alpha$  at  $\pi$  and  $\sigma$  polarisations, respectively.

### 288 **Multiplet ligand-field calculations**

289 The crystal field multiplet model is an effective model Hamiltonian for the description of all charge  
290 conserving excitations of ionic transition metal systems. The crystal field multiplet model is valid  
291 for the main peaks of  $2p$  x-ray absorption and the low-energy RIXS excitations of ionic transition  
292 metal ions, because the  $2p3d$  x-ray absorption and the  $3d2p$  x-ray emission are neutral, self-  
293 screened, transitions, which implies that screening channels such as ligand-metal charge transfer  
294 can be approximated by renormalized parameters. We used the quantum many-body program  
295 Quanty (26) to simulate Fe XAS and  $2p3d$  RIXS in  $\alpha$ -Fe<sub>2</sub>O<sub>3</sub>. The Hamiltonian used for the  
296 calculations consists of the following terms: (i) Coulomb interaction, (ii) crystal field potential, (iii)  
297 spin-orbit coupling, and (iv) effective exchange interaction. The  $d-d$  ( $p-d$ ) multipole part of the  
298 Coulomb interaction was scaled to 70% (80%) of the Hartree-Fock values of the Slater integral.  
299 The general parameters used for the simulations agree with previous studies of  $\alpha$ -Fe<sub>2</sub>O<sub>3</sub> L<sub>2,3</sub> edges.

### 300 **Expression of the effective RIXS operator**

301 The effective operator can be expressed by equation (3) as shown by Haverkort (22). Here  $\epsilon_{in(out)}$   
302 is the incoming (outgoing) polarization of the photons.  $F_{\{x,y,z\}}$  is the conductivity tensor describing  
303 the full magneto-optical response function of the system depending on the local magnetization  
304 direction given by  $\{x, y, z\}$ .

$$305 \quad R_{eff} = -\text{Im}[\epsilon_{in}^* \cdot F_{\{x,y,z\}} \cdot \epsilon_{out}] \quad (3)$$

306 The general form of the conductivity tensor can be expressed as a sum of linear independent spectra  
307 multiplied by functions depending on the local magnetization direction as given in equation (4).

$$308 \quad F_{\{x,y,z\}} = \sum_{k=0}^{\infty} \sum_{m=-k}^k \begin{pmatrix} F_{xx}^{k,m} & F_{xy}^{k,m} & F_{xz}^{k,m} \\ F_{yx}^{k,m} & F_{yy}^{k,m} & F_{yz}^{k,m} \\ F_{zx}^{k,m} & F_{zy}^{k,m} & F_{zz}^{k,m} \end{pmatrix} Y_{k,m}(\theta, \phi) \quad (4)$$

309 Here  $\theta$  and  $\phi$  define the direction of the local moment with  $\theta$  being the polar angle, and  $\phi$  being  
310 the azimuthal angle.  $Y_{k,m}(\theta, \phi)$  is a spherical harmonic function and  $F_{ij}^{k,m}$  is the  $i,j$  component of  
311 the conductivity tensor on a basis of linear polarized light in the coordinate system of the crystal.  
312 In symmetries lower than spherical, this expansion on spherical harmonics does not truncate at  
313 finite  $k$  and the angular momentum of the electrons only is not a conserved quantum number in the  
314 crystals. We have shown in our previous work that including terms up to  $k = 3$  is sufficient to  
315 describe Fe<sup>3+</sup> ions in octahedral crystal field (27). The expression is given in equation (5) and  
316 involves terms up to the 3<sup>rd</sup> order in spin leading to single, double, and triple spin flip processes.



$$F_{\{x,y,z\}} = \begin{pmatrix} F_{a1g}^0 + 2F_{eg}^2(S_x^2 - \frac{1}{3}S^2) & F_{t2g}^2(S_xS_y + S_yS_x) - F_{t1u}^1S_z - F_{t1u}^3(-\frac{3S_z}{5} + S_z^3) & F_{t1u}^1S_y + F_{t1u}^3(-\frac{3S_y}{5} + S_y^3) + F_{t2g}^2(S_xS_z + S_zS_x) \\ F_{t2g}^2(S_y + S_yS_x) + F_{t1u}^1S_z + F_{t1u}^3(-\frac{3S_z}{5} + S_z^3) & F_{a1g}^0 + 2F_{eg}^2(S_y^2 - \frac{1}{3}S^2) & -F_{t1u}^1S_x - F_{t1u}^3(-\frac{3S_x}{5} + S_x^3) + F_{t2g}^2(S_yS_z + S_zS_y) \\ -F_{t1u}^1S_y - F_{t1u}^3(-\frac{3S_y}{5} + S_y^3) + F_{t2g}^2(S_xS_z + S_zS_x) & F_{t1u}^1S_x + F_{t1u}^3(-\frac{3S_x}{5} + S_x^3) + F_{t2g}^2(S_yS_z + S_zS_y) & F_{a1g}^0 + 2F_{eg}^2(S_z^2 - \frac{1}{3}S^2) \end{pmatrix} \quad (5)$$

317

318 **Data availability**

319 The data generated and analyzed are included in the paper and its supplementary  
 320 information and have been all deposited in the zenodo database under accession code  
 321 at <https://zenodo.org/record/7828290>. Raw data files will be made available upon request.

322 **Code availability**

323 The code that supports the findings of this study is available online and can be downloaded  
 324 at: <https://www.quanty.org> together with a full documentation and instructions to use it. The  
 325 script file required to reproduce the theoretical figures has been deposited in the zenodo  
 326 database under accession code at <https://zenodo.org/record/7828290>.

327 **References**

- 328 1. F. Bloch, Zur Theorie des Austauschproblems und der Remanenzerscheinung der  
 329 Ferromagnetika. *Z. Phys.* **74**, 295-335 (1939).
- 330 2. K. Zakeri, Terahertz magnonics: Feasibility of using terahertz magnons for information  
 331 processing. *Phys. C: Supercond. Appl.* **549**, 164-170 (2018).
- 332 3. A. Safin, S. Nikitov, A. Kirilyuk, D. V. Kalyabin, A. Sadovnikov, P. Stremoukhov, M.  
 333 Logunov, P. Popov, Excitation of terahertz magnons in antiferromagnetic nanostructures:  
 334 Theory and experiment. *J. Exp. Theor. Phys* **131**, 71-82 (2020).
- 335 4. V. Kruglyak, S. Demokritov, D. Grundler, Magnonics. *J. Phys. D: Appl. Phys.* **43**, 260301  
 336 (2010).
- 337 5. F. de Groot, P. Kuiper, and G. Sawatzky, Local spin-flip spectral distribution obtained by  
 338 resonant x-ray Raman scattering, *Phys. Rev. B.* **57**, 14584 (1998).
- 339 6. L. Ament, M. van Veenendaal, T. Devereaux, J. Hill, J. van den Brink, Resonant inelastic  
 340 x-ray scattering studies of elementary excitations. *Rev. Mod. Phys.* **83**, 705-767 (2011).
- 341 7. M. Dean, R. Springell, C. Monney, K.-J. Zhou, J. Pereiro, I. Božović, B. Dalla Piazza, H.  
 342 Rønnow, E. Morenzoni, J. van den Brink, T. Schmitt, J. Hill, Spin excitations in a single  
 343 La<sub>2</sub>CuO<sub>4</sub> layer. *Nat. Mater.* **11**, 850-854 (2012).
- 344 8. Y. Peng, G. Dellea, M. Minola, M. Conni, A. Amorese, D. Di Castro, G. De Luca, K.  
 345 Kummer, M. Salluzzo, X. Sun, X. Zhou, G. Balestrino, M. Le Tacon, B. Keimer, L.  
 346 Braicovich, N. Brookes, G. Ghiringhelli, Influence of apical oxygen on the extent of in-  
 347 plane exchange interaction in cuprate superconductors. *Nat. Phys.* **13**, 1201-1206 (2017).
- 348 9. J. Kim, D. Casa, M. Upton, T. Gog, Y.-J. Kim, J. Mitchell, M. van Veenendaal, M.  
 349 Daghofer, J. van den Brink, G. Khaliullin, and B. Kim, Magnetic excitation spectra of  
 350 Sr<sub>2</sub>IrO<sub>4</sub> probed by resonant inelastic x-ray scattering: Establishing links to cuprate  
 351 superconductors. *Phys. Rev. Lett.* **108**, 177003 (2012).
- 352 10. M. Dean, Y. Cao, X. Liu, S. Wall, D. Zhu, R. Mankowsky, V. Thampy, X. Chen, J. Vale,  
 353 D. Casa, J. Kim, A. Said, P. Juhas, R. Alonso-Mori, J. Glowia, A. Robert, J. Robinson,  
 354 M. Sikorski, S. Song, M. Kozina, H. Lemke, L. Patthey, S. Owada, T. Katayama. M.  
 355 Yabashi, Y. Tanaka, T. Togashi, J. Liu, C. Rayan Serrao, B. Kim, L. Huber, D.  
 356 McMorrow, M. Först, J. Hill, Ultrafast energy- and momentum-resolved dynamics of

- 357 magnetic correlations in the photo-doped Mott insulator Sr<sub>2</sub>IrO<sub>4</sub>. *Nat. Mater.* **15**, 601-605  
358 (2015).
- 359 11. H. Robarts, M. García-Fernández, J. Li, A. Nag, A. Walters, N. Headings, S. Hayden, K.-  
360 J. Zhou, *Phys. Rev. B.* **103**, 224427 (2021).
- 361 12. G. Ghiringhelli, A. Piazzalunga, C. Dallera, T. Schmitt, V.N. Strocov, J. Schlappa, L.  
362 Patthey, X. Wang, H. Berger, M. Grioni, Observation of two nondispersive magnetic  
363 excitations in NiO by resonant inelastic soft-X-ray scattering. *Phys. Rev. Lett.* **102**, 027401  
364 1-4 (2009).
- 365 13. A. Nag, H. Robarts, F. Wenzel, J. Li, H. Elnaggar, R.-P. Wang, A. Walters, M. García-  
366 Fernández, F. de Groot, M. W. Haverkort, K.-J. Zhou, Many-body physics of single and  
367 double spin-flip excitations in NiO. *Phys. Rev. Lett.* **124**, 067202 (2020).
- 368 14. L. Chaix, E. Huang, S. Gerber, X. Lu, C. Jia, Y. Huang, D. McNally, Y. Wang, F. Vernay,  
369 A. Keren, M. Shi, B. Moritz, Z.-X. Shen, T. Schmitt, T. Devereaux and W.-S. Lee,  
370 Resonant inelastic x-ray scattering studies of magnons and bimagnons in the lightly doped  
371 cuprate La<sub>(2-x)</sub>Sr<sub>x</sub>CuO<sub>4</sub>. *Phys. Rev. B.* **97**, 155144 (2018).
- 372 15. K.-J. Zhou,\* A. Walters, M. Garcia-Fernandez, Th. Rice, M. Hand, A. Nag, J. Li, S.  
373 Agrestini, P. Garland, H. Wang, S. Alcock, I. Nistea, B. Nutter, N. Rubies, G. Knap, M.  
374 Gaughran, F. Yuan, P. Chang, J. Emmins and G. Howell, I21: an advanced high-resolution  
375 resonant inelastic x-ray scattering beamline at Diamond Light Source. *J. Synchrotron Rad.*  
376 **29**, 563-580 (2022).
- 377 16. P. Kuiper, B. Searle, P. Rudolf, L. Tjeng, C. Chen, X-ray magnetic dichroism of  
378 antiferromagnet Fe<sub>2</sub>O<sub>3</sub>: The orientation of magnetic moments observed by Fe 2p x-ray  
379 absorption spectroscopy. *Phys. Rev. Lett.* **70**, 1549-1552 (1993).
- 380 17. P. Miedema and F. de Groot, The iron L edges: Fe 2p x-ray absorption and electron  
381 energy loss spectroscopy. *J. Electron Spectros. Relat. Phenomena*, **187**, 32-48 (2013).
- 382 18. J. Miyawaki, S. Suga, H. Fujiwara, M. Urasaki, H. Ikeno, H. Niwa, H. Kiuchi, Y. Harada.  
383 Dzyaloshinskii-Moriya interaction in  $\alpha$ -Fe<sub>2</sub>O<sub>3</sub> measured by magnetic circular dichroism in  
384 resonant inelastic soft x-ray scattering. *Phys. Rev. B*, **96**, 214420 (2017).
- 385 19. E. Samuelsen, G. Shirane, Inelastic neutron scattering investigation of spin waves and  
386 magnetic interactions in Fe<sub>2</sub>O<sub>3</sub>. *Phys. Stat. Sol.* **42**, 241-256 (1970).
- 387 20. A. Nag, A. Nocera, S. Agrestini, M. Garcia-Fernandez, A. C. Walter, S.-W. Cheong, S.  
388 Johnston, K.-J. Zhou, Quadrupolar magnetic excitations in an isotropic spin-1  
389 antiferromagnet. *Nat. Commun.* **13**, 2327 (2022).
- 390 21. S. Streib, Difference between angular momentum and pseudoangular momentum. *Phys.*  
391 *Rev. Lett.* **103**, L100409 (2021).
- 392 22. M. W. Haverkort, Theory of resonant inelastic x-ray scattering by collective magnetic  
393 excitations. *Phys. Rev. Lett.* **105**, 167404 (2010).
- 394 23. R.-P. Wang, H. Elnaggar, Ch. J. Titus, K. Tomiyasu, J. Geessinck, G. Koster, F. Frati, J.  
395 Okamoto, D.-J. Huang, F. de Groot, Saturation and self-absorption effects in the angle-  
396 dependent 2p3d resonant inelastic X-ray scattering spectra of Co<sup>3+</sup>. *J. Synchrotron Rad.*  
397 **27**, 1-9 (2020).
- 398 24. J. Miyawaki, S. Suga, H. Fujiwara, M. Urasaki, H. Ikeno, H. Niwa, H. Kiuchi, Y. Harada,  
399 Dzyaloshinskii-Moriya interaction in  $\alpha$ -Fe<sub>2</sub>O<sub>3</sub> measured by magnetic circular dichroism  
400 in resonant inelastic soft x-ray scattering, *Phys. Rev. B.* **96**, 214420 (2017).
- 401 25. F. de Groot, H. Elnaggar, F. Frati, R.P. Wang, M. U. Delgado-Jaime, M. van eenendaal, J.  
402 Fernandez-Rodriguez, M. W. Haverkort, R. J. Green, G. van der Laan, Y. Kvashnin, A.  
403 Hariki, H. Ikeno, H. Ramanantoanina, C. Daul, B. Delley, M. Odelius, M. Lundberg, O.  
404 Kuhn, S. I. Bokarev, E. Shirley, J. Vinson, K. Gilmore, M. Stener, G. Fronzoni, P.  
405 Decleva, P. Kruger, M. Retegan, Y. Joly, Ch. Vorwerk, C. Draxl, J. Rehr, A. Tanaka, 2p x-

- 406 ray absorption spectroscopy of *3d* transition metal systems, *J. Electron Spectros. Relat.*  
407 *Phenomena*, **249**, 147061 (2021).
- 408 26. M. W. Haverkort, M. Zwierzycki, O. K. Andersen, Multiplet ligand-field theory using  
409 Wannier orbitals. *Phys. Rev. B* **58**, 165113 (2012).
- 410 27. H. Elnaggar, M. W. Haverkort, M. H. Hamed, S. S. Dhesi and F. de Groot, Tensor  
411 description of X-ray magnetic dichroism at the Fe L<sub>2,3</sub>-edges of Fe<sub>3</sub>O<sub>4</sub>. *J. Synchrotron*  
412 *Rad.* **28**, 247–258 (2021).

413 **Acknowledgments**

414 We acknowledge the staff of beamline I21 of Diamond Light Source for their help in setting  
415 up and running the experiments. We acknowledge the following fundings:  
416 Dutch Research Council Rubicon Fellowship (Project No. 019.201EN.010): HE  
417 ERC advanced Grant XRAYonACTIVE No. 340279: FdG

418 **Author Contributions Statement:**

419 Conceptualization: HE, FdG  
420 Methodology: HE, FdG, RW, AN, KJZ  
421 Investigation: AN, KJZ, MGF, AW  
422 Visualization: HE, FdG, MWH  
423 Writing—original draft: HE  
424 Writing—review & editing: HE, FdG, MWH, KJZ

425  
426 Correspondence and requests for materials should be addressed to Hebatalla Elnaggar, Ke-  
427 Jin Zhou, and Frank de Groot.

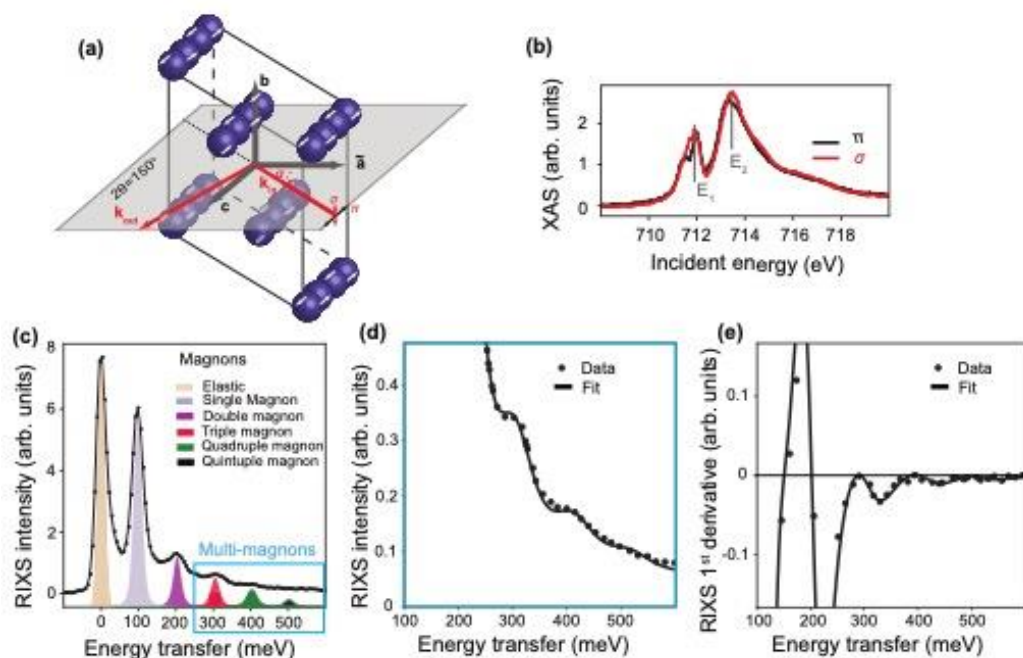
428  
429 **Competing Interests Statement:**

430 The authors declare no competing interests.

431

432  
433  
434

Figure Legends/Captions (for main text figures):



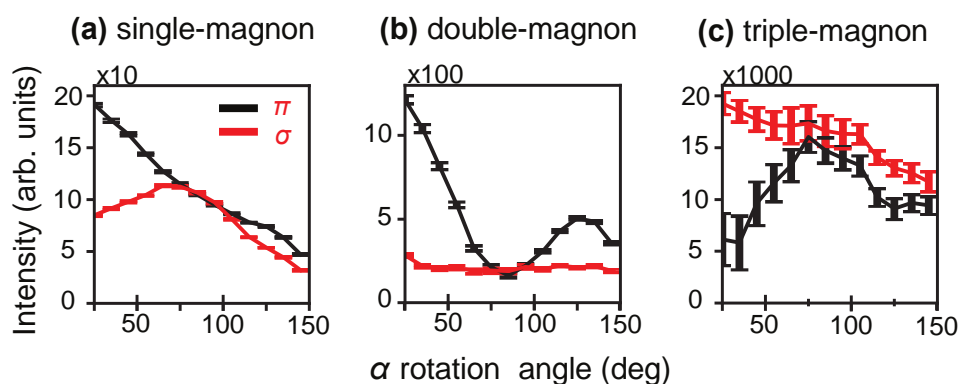
435  
436

**Fig. 1. Crystal structure and x-ray L<sub>3</sub>-edge measurements in a (0001)  $\alpha$ -Fe<sub>2</sub>O<sub>3</sub> single crystal.**

437  
438  
439  
440  
441  
442  
443  
444  
445  
446  
447  
448  
449  
450  
451  
452  
453

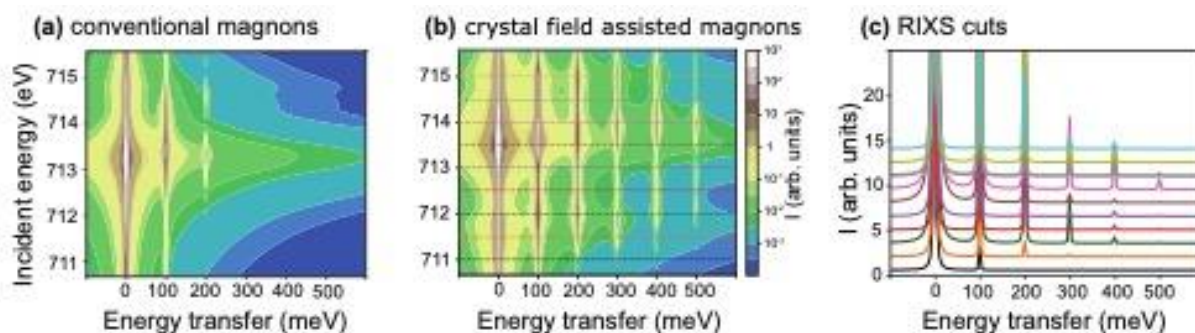
(a) Crystal structure of  $\alpha$ -Fe<sub>2</sub>O<sub>3</sub> showing only the Fe atoms and the scattering geometry used for all measurements presented in this work.  $\mathbf{k}_{in(out)}$  are the incident and outgoing wave vectors and the scattering angle ( $2\theta$ ) was kept fixed at 150°. The incidence angle is  $\alpha$  with  $\alpha = 90^\circ$  for normal incidence. The antiferromagnetic order is depicted with white arrows showing the orientation of the magnetic moments. (b) Fe L<sub>3</sub> XAS measured with  $\pi$  (black) and  $\sigma$  (red) polarization. Two main peaks can be identified and are labelled E<sub>1</sub> and E<sub>2</sub>. (c) RIXS spectra measured at E<sub>1</sub> ( $\alpha = 95^\circ$ ,  $\pi$  polarization). The orange shaded Gaussian peak at zero energy transfer corresponds to the elastic peak also having contribution from  $\Delta M_S=0$  excitation. The five shaded antisymmetric Lorentzian peaks represent the single- (blue), double- (purple), triple- (red), quadrupole- (green) and quintuple- (black) magnon excitations (see Methods for the fitting details). The blue box highlights the spin non-conserving transitions. (d) A zoom on the spin non-conserving transitions. The dots are experimental data, and the black line is the fit. The triple- and quadrupole -magnons can be clearly identified. (e) The first derivative of panel (d) where the signal equals zero at the position of the higher-rank magnons.

454  
455  
456  
457



459  
460  
461  
462  
463  
464  
465

**Fig. 2. Angular dependence of the magnons measured with  $\pi$  and  $\sigma$  polarization.** (a) Single-magnon, (b) double-magnon and (c) triple-magnon excitations measured at the incidence energy  $E_1$ . The angular dependence is measured by rotating the single crystal in the azimuthal direction ( $\alpha$  rotation) while the scattering angle was kept fixed at  $150^\circ$ . The error bars shown are least square fitted intensity value errors.



466  
467  
468  
469  
470  
471  
472  
473  
474  
475  
476

**Fig. 3. Full-multiplet ligand field theory calculation for  $\text{Fe}^{3+}$   $L_3$ -edge RIXS in  $\alpha\text{-Fe}_2\text{O}_3$ .** (a) Incident energy dependent RIXS intensity map for an  $\text{Fe}^{3+}$  ion according to the Hamiltonian in Equation 1. (b) Considering an additional term that includes the crystal field effects. The calculations were performed for linear horizontal incoming beam and unpolarized outgoing beam to correspond to the experimental conditions. The parameters used for the calculations are reported in SI Tab. 1. We note that the intensity is plotted in a logarithmic scale. (c) Line cuts through the RIXS map of panel (b) plotted at the dashed lines positions shown on the map.

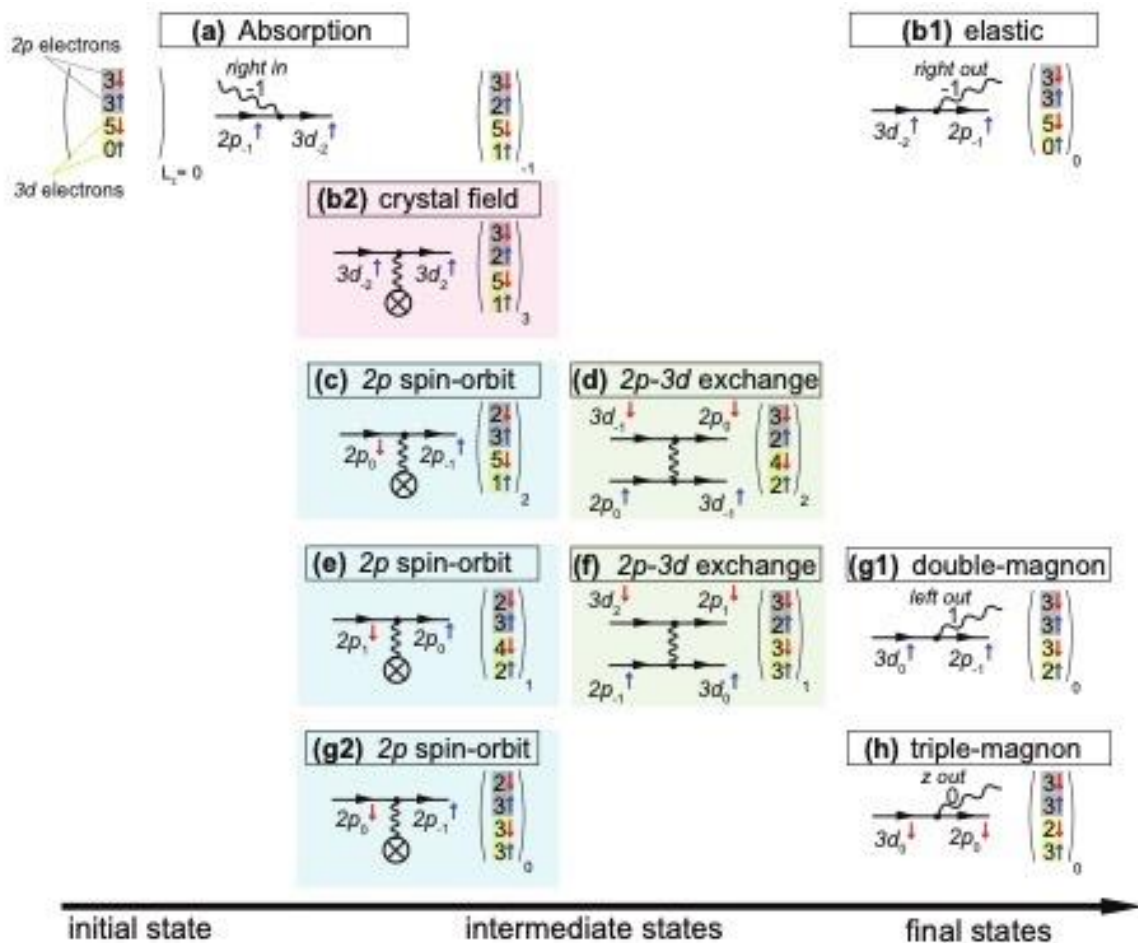
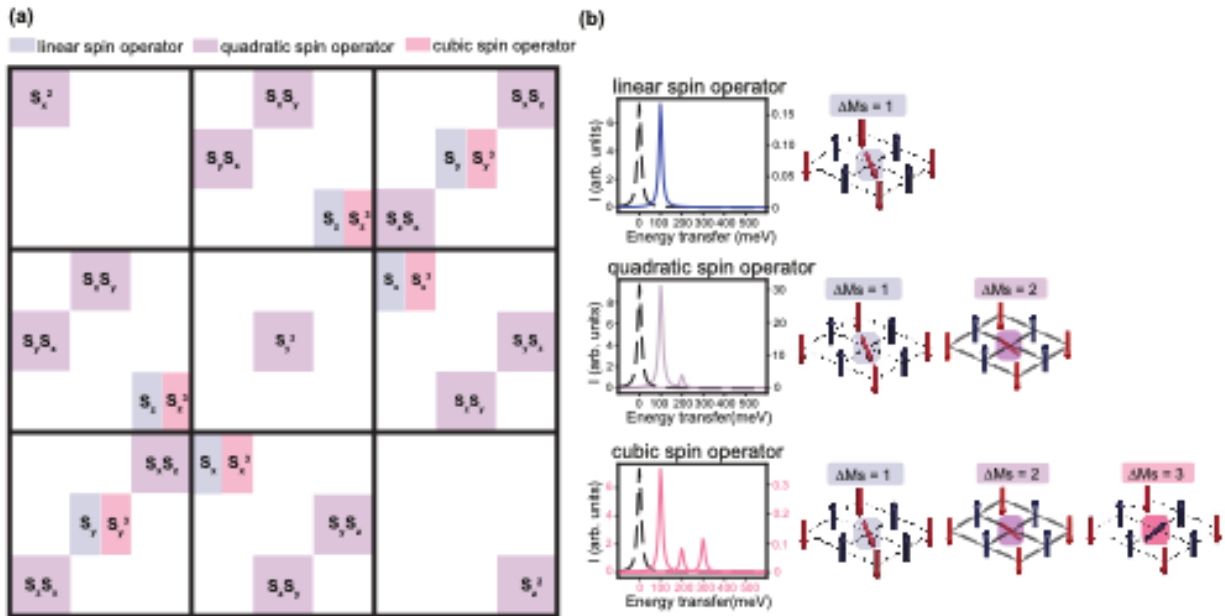
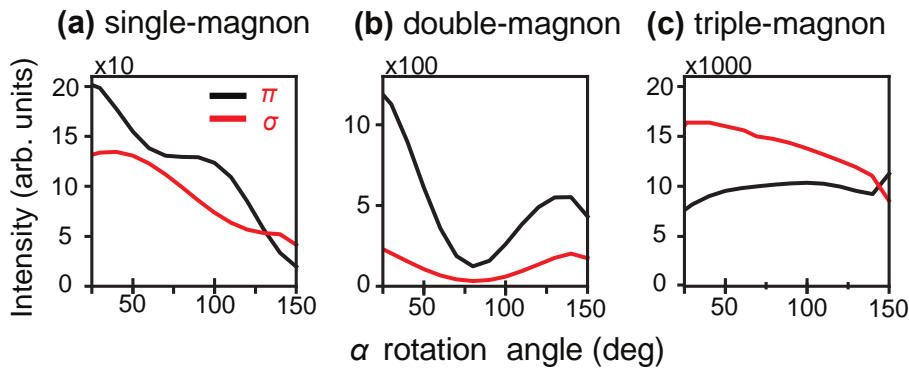


**Fig. 4. Schematic representation of the mechanism of higher-rank magnons by  $2p3d$  RIXS.** The initial state vector is shown in the upper left corner comprising of the  $2p$  (gray) and  $3d$  (yellow) orbitals participating in the RIXS process. The spin of the electrons is depicted by the colored arrows (red = down, blue = up). We follow the fate of a  $2p \rightarrow 3d$  excitation created by the absorption of a right polarized photon (a) up to the triple-magnon decay through a cascade of crystal field interaction,  $2p$  spin-orbit coupling and  $2p$ - $3d$  exchange interaction through the steps from (b) to (h).



487  
488  
489  
490  
491  
492  
493  
494

**Fig. 5. Matrix elements of the effective RIXS operator ( $R_{\text{eff}}$ ) expanded up to the third rank and the RIXS spectrum from individual operators. (a) A summary of the expansion presented in equation 3 grouped in terms of linear (blue), quadratic (purple) and cubic (red) spin operators ( $S$ ) involved in the RIXS cross-section. (b) The RIXS cross-section computed using the three orders of the spin operators.**



495  
496  
497  
498  
499

**Fig. 6. Computed angular dependence of the magnons measured with  $\pi$  and  $\sigma$  polarization using the effective operator expansion. (a) Single-magnon, (b) double-magnon and (c) triple-magnon excitations at the incidence energy  $E_1$ .**